

Consistent \overline{C} Element-Free Galerkin Method for Finite Strain Analysis



P. Areias, F. Carapau , J. Carrilho Lopes, and T. Rabczuk

1 Introduction

Simulations of engineering material processing technology are supported by elastoplastic analyses. Two constitutive requirements are important in this context: (1) the quality of the stress values present in the yield functions depends on the smoothness of the displacements and crucially on mesh distortion [1] and (2) quasi-incompressibility conditions in metal plasticity and polymers are difficult to satisfy with reasonable support sizes in meshless methods [2]. Compared with displacements, errors in stresses are a magnitude higher, even without accounting for incompressibility. High-order (quadratic and cubic) finite elements are typically not adopted in finite strain elastoplastic analysis due to well-known shortcomings:

- High-order elements are adversely impacted by mesh distortion. Convergence rate is changed by distortion [1]. Adaptive remeshing is required more often with high-order elements.
- Problems requiring high-order derivatives impose dedicated techniques or isogeometric formulations [3].

P. Areias

Instituto Superior Técnico, Lisbon, Portugal

e-mail: pedro.areias@tecnico.ulisboa.pt

F. Carapau (✉) · J. C. Lopes

Universidade de Évora, Colégio Luis António Verney, Évora, Portugal

e-mail: flc@uevora.pt

T. Rabczuk

Bauhaus-University Weimar, Weimar, Germany

e-mail: timon.rabczuk@uni-weimar.de

- Although stress quality improves with the order of the complete polynomial, in finite element methods, stresses are still discontinuous at inter-element boundaries [4]. Plasticity results are dependent on the quality of the stresses, which is compromised even in high-order finite elements.
- The use of finite elements for quasi-incompressible problems requires specialized techniques (see, for example, [5–7]).

Note that Rabczuk, Belytschko, and Xiao [8] proved that a Lagrangian kernel is required for stability,¹ but classical finite strain plasticity algorithms (e.g., [9, 10]) combined with EFG are based on configuration updating (see [11]). A comprehensive presentation of developments in meshless methods (including EFG) was recently published by J.-S. Chen et al. [12]. A related development combining partition of unity and least squares is described in Cai et al. [13]. Several remedies are described, in particular for boundary conditions. Therefore, meshless methods, in particular with quadratic and cubic bases and satisfying the Kronecker delta condition, perfectly fit these applications:

- Since no isoparametric mapping is used, mesh distortion sensitivity is attenuated with respect to finite elements.
- Stresses are continuous, as long as all terms participating in the shape functions are differentiable.
- Contact algorithms are relatively simplified.
- Quasi-incompressibility can be directly addressed by changing the polynomial basis.
- Strain localization problems can be directly addressed via strain-gradient methods.

Several applications have been published with meshless discretization for finite strain plasticity [11], but not at the same scale of finite elements. The reputation for difficult-to-impose boundary conditions still affects EFG, although developments in interpolation have resurrected interest in the question of the Kronecker delta property (see [14]). In contrast with finite strain plasticity, hyperelastic implementations of EFG are common, and recent papers report realistic results with high degree of continuity (see [15]). In this paper are the following:

A newly developed fully anisotropic elastoplastic framework based on the iteration for C_e [16] does not require the explicit form of the deformation gradient. This motivates a revisiting of the moving least squares/EFG approach. Another effect that is often reported in the context of EFG is the volumetric locking in quasi-incompressible applications, [11, 17]. This is addressed here by the following techniques:

- Selective quadrature for the right Cauchy-Green tensor C , with reduced quadrature in $\det C$ and full quadrature in $\widehat{C} = \det[C]^{-1/3} C$

¹ Strictly in particle methods, but stabilized particle methods share properties with EFG.

- Selective interpolation for these terms, with a higher-order polynomial being adopted for \bar{C}

In terms of discretization, this work adopts the following techniques:

- Ab initio definition of the shape functions and derivatives for the entire analysis.
- Parameterized quadrature and interpolation functions for the deviatoric and volumetric parts of the right Cauchy-Green tensor C .
- Quasi-singular weight functions (see [18–20]).
- Quadrature points are defined in tetrahedra.
- Lagrangian diffuse derivatives are adopted.
- Constitutive integration making use of the Mandel stress tensor and iteration on C_e [16].

Volumetric locking has been diagnosed in element-free Galerkin methods by Dolbow and Belytschko [21] where a mixed displacement-pressure formulation was proposed in the small strain case. Within the RKPM family of W.K. Liu's group, a pressure projection method was proposed, where pressure is re-interpolated using fewer points and a specific patch [22]. Applications were made with incompressible hyperelasticity. More conventional F-bar formulations have been used in the context of particle methods with explicit integration by Wu et al. [23]. In the small strain case, Recio, Jorge and Dinis [24] have applied \bar{B} and Enhanced strain techniques to an EFG formulation. For implicit integration, an incremental finite deformation version was adopted by Coombs et al. [25]. In neither of these papers the closed-form expressions for the equilibrium and Jacobian were presented in the finite strain case. In the incremental case (see [25]), expressions are significantly simplified, and results for moderate plastic deformations are shown in that paper. In Moutsanidis et al. [26], an F-bar implementation is presented for the conforming reproducing kernel method. Navas et al. [27], in order to avoid the locking involved in the fluid phase of the porous media, devised a B-bar algorithm.

This paper is organized as follows: Sect. 2 presents the interpolation, based on moving least squares and diffuse derivatives, as well as the algorithm to guarantee a sufficiently small support radius. Section 3 presents the discretization based on the total Lagrangian approach, including the partition of C with its first and second variations. This is followed by Sect. 4 where the constitutive integration, fitting the developments of Sect. 3, is described in detail. In Sect. 5, three benchmark tests are presented, and finally conclusions are drawn in Sect. 6.

2 Interpolation

2.1 General Approach for Moving Least Squares

Interpolation with a polynomial basis and least squares fitting was introduced by P. Lancaster and K. Salkauskas [18]. Herein, classical derivations are followed (see

[19, 28, 29]). We introduce m as the number of terms in the polynomial basis, n as the number of supporting nodes, and D as support radius. For a given node K , the distance to a given point with coordinates \mathbf{X} is identified as $s_K(\mathbf{X})$. Let us consider a q -tuple of nonnegative integers $\boldsymbol{\alpha} = (\alpha_1, \dots, \alpha_q) \in \mathbb{N}_0^q$. We write the absolute value as the sum $|\boldsymbol{\alpha}| = \sum_{i=1}^q \alpha_i$. We consider the set of all polynomials of degree equal or less than p as:

$$\mathcal{P}_p = \left\{ p_{\boldsymbol{\alpha}}(\mathbf{X}) = X_1^{\alpha_1} \cdots X_q^{\alpha_q} \mid |\boldsymbol{\alpha}| \leq p \right\}. \quad (1)$$

We now introduce a polynomial basis as an array of elements of \mathcal{P}_p :

$$\mathbf{p}(\mathbf{X}) = \{p_1(\mathbf{X}), p_2(\mathbf{X}), \dots, p_m(\mathbf{X})\} \quad p_i \in \mathcal{P}_p \quad (2)$$

with $\#\mathbf{q}(\mathbf{X}) = (p+q)!/p!q! = m$. We therefore use m elements of \mathcal{P} for the polynomial basis. The direct form (2) is known to produce conditioning difficulties. Therefore, we adopt a normalized and shifted form using a complete basis:

$$\begin{aligned} p(\mathbf{X}) = \left\{ 1, \frac{(X_1 - \bar{X}_1)}{D}, \frac{(X_2 - \bar{X}_2)}{D}, \frac{(X_3 - \bar{X}_3)}{D}, \right. \\ \left. \frac{(X_1 - \bar{X}_1)(X_2 - \bar{X}_2)}{D^2}, \frac{(X_1 - \bar{X}_1)(X_3 - \bar{X}_3)}{D^2}, \frac{(X_2 - \bar{X}_2)(X_3 - \bar{X}_3)}{D^2}, \right. \\ \left. \frac{(X_1 - \bar{X}_1)^2}{D^2}, \frac{(X_2 - \bar{X}_2)^2}{D^2}, \frac{(X_3 - \bar{X}_3)^2}{D^2}, \dots \right\}. \quad (3) \end{aligned}$$

We use $\bar{\mathbf{X}}$ as a centroid of the nodes within the D -radius of \mathbf{X} . Given a point with coordinates \mathbf{X} , the approximation weight of another point with coordinates \mathbf{X}_I depends on the distance between the points $s_I(\mathbf{X}) = \|\mathbf{X} - \mathbf{X}_I\|$. The notation $w[s_I(\mathbf{X})]$ is introduced to represent this weight function of \mathbf{X} . From this basis, an $m \times n$ \mathbf{P} Vandermonde matrix is defined by its elements as follows:

$$P_{iJ} = p_i(\mathbf{X}_J) \quad i = 1, \dots, m, \quad J = 1, \dots, n \quad (4)$$

The components of weight matrix, which is a function of the supporting points and the coordinates \mathbf{X} , are given by:

$$W_{IJ}(\mathbf{X}) = \delta_{IJ} w[s_I(\mathbf{X})] \quad I, J = 1, \dots, n \quad (5)$$

Applying the traditional least squares arguments [28] leads to the following format for the n -dimensional shape function array $\mathbf{N}(\mathbf{X})$:

$$\mathbf{N}(\mathbf{X}) = \mathbf{p}(\mathbf{X}) \cdot \mathbf{A}^{-1}(\mathbf{X}) \cdot \mathbf{B}(\mathbf{X}) \quad (6)$$

where $\mathbf{A}(\mathbf{X})$ is the $m \times m$ moment matrix $\mathbf{A}(\mathbf{X}) = \mathbf{B}(\mathbf{X}) \cdot \mathbf{P}^T$ and $\mathbf{B}(\mathbf{X})$ is the $m \times n$ linear combination matrix $\mathbf{B}(\mathbf{X}) = \mathbf{P} \cdot \mathbf{W}(\mathbf{X})$. We make use of the $\mathbf{Q} \cdot \mathbf{R}$ decomposition of $\sqrt{\mathbf{W}(\mathbf{X})} \cdot \mathbf{P}^T$:

$$\sqrt{\mathbf{W}(\mathbf{X})} \cdot \mathbf{P}^T = \mathbf{Q}(\mathbf{X}) \cdot \mathbf{R}(\mathbf{X}) \quad (7)$$

where $\mathbf{Q}(\mathbf{X})$ is an orthogonal matrix and $\mathbf{R}(\mathbf{X})$ is an upper triangular matrix [30]. A classical Gram-Schmidt algorithm for the $\mathbf{Q} \cdot \mathbf{R}$ decomposition is used (see [31]). For our application, only $\mathbf{R}(\mathbf{X})$ is required. It is straightforward to obtain, from (6), the final form of the shape function array:

$$\mathbf{N}(\mathbf{X}) = \mathbf{p}(\mathbf{X}) \cdot \mathbf{R}^{-1}(\mathbf{X}) \cdot \mathbf{R}^{-T}(\mathbf{X}) \cdot \mathbf{B}(\mathbf{X}). \quad (8)$$

Therefore, this operation is relatively inexpensive since it consists of two triangular solves. Omitting the dependence on \mathbf{X} , we have:

$$\mathbf{R}^T \cdot \mathbf{U}_1 = \mathbf{B} \quad (9)$$

$$\mathbf{R} \cdot \mathbf{U}_2 = \mathbf{U}_1 \quad (10)$$

where \mathbf{U}_2 is a $m \times n$ matrix, which suffices to define the shape functions. Reintroducing the dependence on \mathbf{X} , the result is:

$$\mathbf{N}(\mathbf{X}) = \mathbf{p}(\mathbf{X}) \cdot \mathbf{U}_2(\mathbf{X}). \quad (11)$$

The interpolated value $\phi(\mathbf{X})$ is obtained by linear combination of nodal values $\boldsymbol{\phi} = \{\phi_1, \phi_2, \dots, \phi_n\}$ $\phi(\mathbf{X}) = \mathbf{N}(\mathbf{X}) \cdot \boldsymbol{\phi}$. In terms of components, Eq. (6) is written as:

$$N_L(\mathbf{X}) = p_j(\mathbf{X}) U_{2jL}(\mathbf{X}) \quad L = 1, \dots, n; \quad j, k = 1, \dots, m \quad (12)$$

First derivative of $N_L(\mathbf{X})$ with respect to coordinates X_m , $m = 1, 2, 3$ is here denoted as:

$$\begin{aligned} N'_L(\mathbf{X}) &= p'_j(\mathbf{X}) U_{2jL}(\mathbf{X}) \\ &\quad - p_j(\mathbf{X}) A_{jl}^{-1}(\mathbf{X}) A'_{lp}(\mathbf{X}) U_{2pL}(\mathbf{X}) \\ &\quad + p_j(\mathbf{X}) A_{jk}^{-1}(\mathbf{X}) B'_{kL}(\mathbf{X}) \end{aligned} \quad (13)$$

where:

$$B'_{kL}(\mathbf{X}) = P_{kJ} W'_{JL}(\mathbf{X}) \quad (14)$$

$$A'_{lp}(\mathbf{X}) = B'_{lL}(\mathbf{X}) P_{pL}. \quad (15)$$

In terms of $p'_j(\mathbf{X})$ and $W'_{jI}(\mathbf{X})$, Eq. (13) can be written as a sum of two terms:

$$N'_L(\mathbf{X}) = N_L^*(\mathbf{X}) + N_L^\bullet(\mathbf{X}) \quad (16a)$$

where:

$$N_L^*(\mathbf{X}) = p'_j(\mathbf{X}) U_{2jL}(\mathbf{X}) \quad (16b)$$

and:

$$N_L^\bullet(\mathbf{X}) = p_j(\mathbf{X}) A_{jl}^{-1}(\mathbf{X}) P_{lM} W'_{MQ}(\mathbf{X}) [\delta_{QL} - P_{pQ} U_{2pL}(\mathbf{X})]. \quad (16c)$$

It is a tradition to identify (16b) as the diffuse derivative (see Nayroles, Touzot, and Villon [32]).

2.2 Quasi-Singular Weight Function

Singular weight functions are known to produce an interpolation satisfying the Kronecker delta property [18]. Quasi-singular functions have been adopted to approximate this property [19]. The following quasi-singular weight function is introduced (see, for example, [19, 20]):

$$w[s_I(\mathbf{X})] = \begin{cases} [s_I^2(\mathbf{X})/D^2 + \text{tol}^2]^{-1} - [1 + \text{tol}^2]^{-1} & s_I \leq D \\ 0 & s_I > D \end{cases} \quad (17)$$

where $\text{tol} \in \mathbb{R}^+$ is a tolerance parameter. The maximum value of $w[s_I]$ is obtained as:

$$w[0] = 1/(\text{tol}^2 + \text{tol}^4). \quad (18)$$

Here, we adopt $\text{tol} = 1 \times 10^{-3}$. The Kronecker delta property is approximately satisfied:

$$N_I(\mathbf{X}_J) \cong \delta_{IJ}. \quad (19)$$

Derivatives of $w[s_I]$ with respect to s_I are trivially given by

$$\frac{dw[s_I]}{ds_I} = -\frac{2D^2 s_I}{(D^2 \text{tol}^2 + s_I^2)^2}. \quad (20)$$

Strong versions of this weighting are available (see M. Dehghan, [33]) but involve an intricate implementation.

3 Discrete Equilibrium Equations

In finite element technology, two papers introduced a consistent formulation for the so-called mean dilatation technique [6, 34] which was invented by Nagtegaal et al. [35]. A straightforward total Lagrangian implementation is followed (see, for example, [36]). We make use of the definition of the right Cauchy-Green tensor:

$$\mathbf{C}(\mathbf{X}_h) = \mathbf{F}^T(\mathbf{X}) \cdot \mathbf{F}(\mathbf{X}). \quad (21)$$

A partition into volumetric and deviatoric parts is required for selective quadrature. Omitting the dependence on \mathbf{X}_h , the deviatoric Cauchy-Green tensor follows from the Flory [37] decomposition:

$$\widehat{\mathbf{C}} = \det[\mathbf{C}]^{-1/3} \mathbf{C}. \quad (22)$$

Introducing the variation symbol δ and taking advantage of the symmetry of \mathbf{C} , the variation of $\widehat{\mathbf{C}}$ is calculated as (see also Appendix Section “First and Second Variations of $\det[\mathbf{C}]$ ”):

$$\delta \widehat{\mathbf{C}} = \left(\det[\mathbf{C}]^{-1/3} \mathcal{I} - \frac{1}{3} \widehat{\mathbf{C}} \otimes \mathbf{C}^{-1} \right) : \delta \mathbf{C} \quad (23)$$

where \mathcal{I} is the symmetric fourth-order identity tensor, i.e., $[\mathcal{I}]_{ijkl} = \frac{1}{2} (\delta_{ij} \delta_{kl} + \delta_{ik} \delta_{jl})$. This variation will be required later in the formation of the weak form of equilibrium. Newton-Raphson iteration requires the second variation of $\widehat{\mathbf{C}}$. For the second variation of $\widehat{\mathbf{C}}$, we adopt the time derivative notation, which results in:

$$\begin{aligned} \delta \dot{\widehat{\mathbf{C}}} &= \left(\det[\mathbf{C}]^{-1/3} \mathcal{I} - \frac{1}{3} \widehat{\mathbf{C}} \otimes \mathbf{C}^{-1} \right) : \delta \dot{\mathbf{C}} \\ &+ \dot{\mathbf{C}} : \left(-\frac{1}{3} \det[\mathbf{C}]^{-4/3} \mathbf{C}^{-1} \otimes \mathcal{I} \right) : \delta \mathbf{C} \\ &+ \dot{\mathbf{C}} : \left(\frac{1}{9} \widehat{\mathbf{C}} \otimes \mathbf{C}^{-1} \otimes \mathbf{C}^{-1} - \frac{1}{3} \det[\mathbf{C}]^{-1/3} \mathcal{I} \otimes \mathbf{C}^{-1} \right) : \delta \mathbf{C} \\ &+ \dot{\mathbf{C}} : \mathbf{T} : \delta \mathbf{C} \end{aligned} \quad (24)$$

where \mathbf{T} is a sixth-order tensor which is defined in terms of components as:

$$[\mathbf{T}]_{mnikl} = \frac{1}{3} C_{km}^{-1} C_{nl}^{-1} \widehat{C}_{ij}. \quad (25)$$

Given the decomposition, we assume an independent $\det[\overline{\mathbf{C}}]$ which we denote as $\theta_C = \det[\overline{\mathbf{C}}]$. In this case, we define a combined right Cauchy-Green tensor:

$$\mathbf{C}_\star = \left(\frac{\theta_C}{\det[\mathbf{C}]} \right)^{1/3} \mathbf{C}. \quad (26)$$

Interpolation for $\overline{\mathbf{C}}$ makes use of a lower-order polynomial and/or fewer quadrature points. The specific form (26) was proposed by Simo et al. [6] with a clear significance: in the context of low-order finite elements, to replace an over-constrained imposition of $\det[\mathbf{C}] \cong 1$ by an independent field θ_C . Here, $\overline{\mathbf{C}}$ can follow a distinct quadrature rule or a distinct interpolation. The first variation of \mathbf{C}_\star is calculated as:

$$\delta \mathbf{C}_\star = \left(\frac{\theta_C}{\det[\mathbf{C}]} \right)^{1/3} \delta \mathbf{C} + \frac{1}{3} \left[(\mathbf{C}_\star \otimes \overline{\mathbf{C}}^{-1}) : \delta \overline{\mathbf{C}} - (\mathbf{C}_\star \otimes \mathbf{C}^{-1}) : \delta \mathbf{C} \right]. \quad (27)$$

Using the time derivative notation, an analogous form is obtained:

$$\dot{\mathbf{C}}_\star = \left(\frac{\theta_C}{\det[\mathbf{C}]} \right)^{1/3} \dot{\mathbf{C}} + \frac{1}{3} \left[(\mathbf{C}_\star \otimes \overline{\mathbf{C}}^{-1}) : \dot{\overline{\mathbf{C}}} - (\mathbf{C}_\star \otimes \mathbf{C}^{-1}) : \dot{\mathbf{C}} \right]. \quad (28)$$

The time derivative of $\delta \mathbf{C}_\star$ is obtained from (27) as:

$$\begin{aligned} \delta \dot{\mathbf{C}}_\star &= -\dot{\theta}_C \frac{2}{9} \theta_C^{-5/3} \widehat{\mathbf{C}} \delta \theta_C - \frac{1}{3} \theta_C^{-2/3} \widehat{\mathbf{C}} \delta \dot{\theta}_C \\ &\quad + \frac{1}{3} \theta_C^{-2/3} \left(\dot{\theta}_C \delta \widehat{\mathbf{C}} + \delta \theta_C \dot{\widehat{\mathbf{C}}} \right) + \theta_C^{1/3} \delta \dot{\widehat{\mathbf{C}}}. \end{aligned}$$

These expressions are error-prone to implement manually and therefore have been implemented in Mathematica [38] with the AceGen add-on, developed by Korelc [39]. The Mathematica sheets and corresponding Fortran 90 source codes are available in GitHub (see [40]). For a given point \mathbf{X}_h with discrete support $\Omega_{\mathbf{X}_h}$, we have:

$$\mathbf{F}(\mathbf{X}_h) = \frac{d\mathbf{x}_h}{d\mathbf{X}_h} = \sum_{L \in \Omega_{\mathbf{X}_h}} \left(\frac{dN_L(\mathbf{X}_h) \mathbf{x}_L}{d\mathbf{X}_h} \right). \quad (29)$$

In terms of components and omitting the dependence on \mathbf{X}_h , we obtain the components of \mathbf{F} as:

$$F_{ij} = \frac{dN_L}{dX_j} x_{iL}. \quad (30)$$

Using the variation symbol, δ , we introduce the variation of \mathbf{F} , in the equilibrium sense, as:

$$\delta F_{ij} = \frac{dN_L}{dX_j} \delta x_{iL}. \quad (31)$$

Introducing the notation $N_{jL} = dN_L/dX_j$ for the shape function derivatives, the following results for \mathbf{C} and its first and second variations are obtained:

$$\begin{aligned} C_{ij} &= N_{iK} N_{jL} x_{kK} x_{kL} \Rightarrow \\ \delta C_{ij} &= N_{iK} N_{jL} (x_{kL} \delta x_{kK} + x_{kK} \delta x_{kL}) \\ \dot{C}_{ij} &= N_{iK} N_{jL} (x_{kL} \dot{x}_{kK} + x_{kK} \dot{x}_{kL}) \\ \delta \dot{C}_{ij} &= N_{iK} N_{jL} (\dot{x}_{kL} \delta x_{kK} + \dot{x}_{kK} \delta x_{kL}). \end{aligned}$$

Note that besides the node indices K and L , the index k is also muted. Equilibrium is established in a weak form by the use of the second Piola-Kirchhoff stress \mathbf{S}_\star and the spatial configuration variation $\delta \mathbf{x}$:

$$\frac{1}{2} \int_{\Omega_0} \mathbf{S}_\star : \delta \mathbf{C}_\star \, d\Omega_0 = \mathbf{f}_{\text{ext}} \cdot \delta \mathbf{x} \quad (32)$$

where $\mathbf{S}_\star \equiv \mathbf{S}_\star(\mathbf{C}_\star)$ where \mathbf{C}_\star was calculated as shown in (27). For the application of Newton-Raphson iteration, we require the first variation of (32). As discussed previously, to avoid confusion with the variation symbol δ , we use the time derivative to denote the variation of equilibrium. By taking this time derivative variation, the tangent modulus \mathcal{C} is employed to read:

$$\frac{1}{2} \int_{\Omega_0} \mathbf{S}_\star : \delta \dot{\mathbf{C}}_\star \, d\Omega_0 + \frac{1}{4} \int_{\Omega_0} \delta \mathbf{C}_\star : \mathcal{C} : \dot{\mathbf{C}}_\star \, d\Omega_0 = \mathbf{f}_{\text{ext}} \cdot \delta \mathbf{x} - \frac{1}{2} \int_{\Omega_0} \mathbf{S}_\star : \delta \mathbf{C}_\star \, d\Omega_0 \quad (33)$$

where \mathbf{f}_{ext} is the external load vector and is the nodal velocity vector. Note that in the implementation, the second derivative of \mathbf{C}_\star is required in $\delta \dot{\mathbf{C}}_\star$. In Voigt form (see [41]), we have the following internal force and tangent stiffness:

$$\mathbf{f}_L = \int_{\Omega_0} \mathbf{B}_L^T \cdot I_6 \cdot \hat{\mathbf{S}}_\star \, d\Omega_0 \quad (34)$$

$$\mathbf{K}_{KL} = \int_{\Omega_0} \mathbf{B}_K^T \cdot I_6 \cdot \mathcal{C} \cdot I_6 \cdot \mathbf{B}_L \, d\Omega_0 + \int_{\Omega_0} \check{\mathbf{S}}_\star \cdot I_6 \cdot \mathbf{B}_L^\star \, d\Omega_0. \quad (35)$$

Matrices \mathbf{B} and \mathbf{B}^* are implemented in [40], and I_6 is a diagonal matrix containing 1 for indices 11 and 22 and 33 and 2 for indices 44, 55, and 66. In contrast with advanced finite element formulations [42, 43], these are classical and direct derivations. In addition, shape functions and corresponding derivatives are calculated once, at the start of the solution process.

4 Hyperelasticity/Plasticity Using the Elastic Mandel Stress Tensor

4.1 Formulation

The Mandel stress tensor approach to finite strain plasticity is adopted [44, 45]. We make use of the Kröner-Lee decomposition [46–48]:

$$\mathbf{F} = \mathbf{F}_e \cdot \mathbf{F}_p. \quad (36)$$

Using (36), the velocity gradient is determined by its definition and then partitioned as follows:

$$\mathbf{L} = \dot{\mathbf{F}} \cdot \mathbf{F}^{-1} = \mathbf{L}_e + \mathbf{F}_e \cdot \mathbf{L}_p \cdot \mathbf{F}_e^{-1} \quad (37)$$

with $\mathbf{L}_e = \dot{\mathbf{F}}_e \cdot \mathbf{F}_e^{-1}$ the elastic velocity gradient and $\mathbf{L}_p = \dot{\mathbf{F}}_p \cdot \mathbf{F}_p^{-1}$ the plastic velocity gradient. The second Piola-Kirchhoff stress is a function of the elastic part of \mathbf{F} by means of $\mathbf{C}_e = \mathbf{F}_e^T \cdot \mathbf{F}_e$ (cf. [49] page 166), the second Piola-Kirchhoff stress at the intermediate configuration is given by $\mathbf{S}_e(\mathbf{C}_e)$ (see [50]), from which energy consistency results in a specific form for the second Piola-Kirchhoff stress $\mathbf{S} = \mathbf{F}_p^{-1} \cdot \mathbf{S}_e(\mathbf{C}_e) \cdot \mathbf{F}_p^{-T}$. In the hyperelastic case, a strain energy density function $\psi(\mathbf{C}_e)$ exists such as:

$$\mathbf{S}_e(\mathbf{C}_e) = 2 \frac{d\psi(\mathbf{C}_e)}{d\mathbf{C}_e}. \quad (38)$$

The Neo-Hookean model is used, with the following strain energy density function:

$$\psi(\mathbf{C}_e) = \frac{\mu}{2} [\text{tr}(\mathbf{C}_e) - 3] - \mu \log \sqrt{\det(\mathbf{C}_e)} + \frac{\lambda}{2} \left[\log \sqrt{\det(\mathbf{C}_e)} \right]^2. \quad (39)$$

The flow law follows similar arguments [45], with the initial plastic deformation gradient corresponding to the identity, $[\mathbf{F}_p]_0 = \mathbf{I}$. Agreeing with standard derivations on plasticity, a yield function ϕ is introduced, as well as a plastic multiplier $\dot{\gamma}$. Introducing the notation $\mathbf{Q}_p = \mathbf{F}_p^{-1}$, we summarize the constitutive system as:

$$\mathbf{S} = \mathbf{Q}_p \cdot \mathbf{S}_e(\mathbf{C}_e) \cdot \mathbf{Q}_p^T \quad (40)$$

$$\dot{\mathbf{Q}}_p = -\dot{\gamma} \mathbf{Q}_p \cdot \mathbf{N}[\mathbf{T}_e] \quad (41)$$

$$[\mathbf{Q}_p]_0 = \mathbf{I} \quad (42)$$

$$\langle \phi(\mathbf{T}_e) + \dot{\gamma} \rangle - \dot{\gamma} = 0 \quad (43)$$

with $\langle \bullet \rangle = \frac{\bullet + |\bullet|}{2}$ being the unit ramp function. In (41), the Mandel stress [44] \mathbf{T}_e is given by:

$$\mathbf{T}_e = \mathbf{C}_e \cdot \mathbf{S}_e(\mathbf{C}_e). \quad (44)$$

Assuming an associated flow law [48], we have the flow vector $\mathbf{N}(\mathbf{T}_e)$ determined from the derivative of $\phi(\mathbf{T}_e)$:

$$\mathbf{N}(\mathbf{T}_e) = d\phi(\mathbf{T}_e)/d\mathbf{T}_e. \quad (45)$$

When hardening is present, power equivalence provides the effective plastic strain rate $\dot{\epsilon}_p$ as a function of the yield stress σ_y :

$$\dot{\epsilon}_p = \dot{\gamma} \frac{\mathbf{T}_e : \mathbf{N}(\mathbf{T}_e)}{\sigma_y}. \quad (46)$$

4.2 Constitutive Integration

For the constitutive integration, we use superscripts n and $n + 1$ to identify two consecutive time steps and Δt as the time step size. Applying the backward Euler method for \mathbf{Q}_p and $\dot{\gamma}$ results in:

$$\mathbf{Q}_p^{n+1} = \mathbf{Q}_p^n \cdot \underbrace{\left[\mathbf{I} + \Delta\gamma \widehat{\mathbf{N}}(\mathbf{C}_e^{n+1}) \right]^{-1}}_{[\Delta \widehat{\mathbf{Q}}(\mathbf{C}_e^{n+1}, \Delta\gamma)]^{-1}} \quad (47)$$

$$\gamma^{n+1} = \gamma^n + \underbrace{\dot{\gamma}^{n+1} \Delta t}_{\Delta\gamma}. \quad (48)$$

We now define the elastic trial Cauchy-Green tensor as $\mathbf{C}_e^* = \left[\mathbf{Q}_p^n \right]^T \cdot \mathbf{C}^{n+1} \cdot \mathbf{Q}_p^n$.

Introducing the function $\widehat{\mathbf{C}}_e^*(\mathbf{C}^{n+1}) = \left(\mathbf{Q}_p^n \right)^T \cdot \mathbf{C}^{n+1} \cdot \mathbf{Q}_p^n$, the constitutive system for $\Delta\gamma > 0$ consists of the following equations:

$$\underbrace{\left[\Delta \widehat{\mathbf{Q}} \left(\mathbf{C}_e^{n+1}, \Delta \gamma \right) \right]^T \cdot \mathbf{C}_e^{n+1} \cdot \left[\Delta \widehat{\mathbf{Q}} \left(\mathbf{C}_e^{n+1}, \Delta \gamma \right) \right] - \widehat{\mathbf{C}}_e^* \left(\mathbf{C}^{n+1} \right)}_{\mathbf{r}_c \left(\mathbf{C}_e^{n+1}, \Delta \gamma, \mathbf{C}^{n+1} \right)} = \mathbf{0} \quad (49)$$

$$\phi_* \left[\mathbf{C}_e^{n+1} \cdot \widehat{\mathbf{S}}_e \left(\mathbf{C}_e^{n+1} \right) \right] = 0. \quad (50)$$

Since \mathbf{C}_e^{n+1} is symmetric, Voigt notation can be used, $\mathbf{C}_e^{n+1} = \text{Voigt}[\mathbf{C}_e^{n+1}]$ and $\mathbf{r}_c \left(\mathbf{C}_e^{n+1}, \Delta \gamma, \mathbf{C}^{n+1} \right) = \text{Voigt} \left[\mathbf{r}_c \left(\mathbf{C}_e^{n+1}, \Delta \gamma, \mathbf{C}^{n+1} \right) \right]$. Omitting the function arguments for conciseness, the Newton-Raphson iteration for \mathbf{C}_e^{n+1} (Voigt form) and $\Delta \gamma$ is written as:

$$\underbrace{\begin{bmatrix} \frac{\partial \mathbf{r}_c}{\partial \mathbf{C}_e^{n+1}} & \frac{\partial \mathbf{r}_c}{\partial \Delta \gamma} \\ \frac{\partial \phi}{\partial \mathbf{C}_e^{n+1}} & 0 \end{bmatrix}}_{\mathbf{J}} \underbrace{\begin{Bmatrix} \Delta \mathbf{C}_e^{n+1} \\ \Delta \Delta \gamma \end{Bmatrix}}_{\Delta \mathbf{Y}} = - \underbrace{\begin{Bmatrix} \mathbf{r}_c \left(\mathbf{C}_e^{n+1}, \Delta \gamma, \mathbf{C}^{n+1} \right) \\ \phi_* \left[\mathbf{C}_e^{n+1} \cdot \widehat{\mathbf{S}}_e \left(\mathbf{C}_e^{n+1} \right) \right] \end{Bmatrix}}_{\mathbf{r}} \quad (51)$$

with $\mathbf{Y} = \left\{ \mathbf{C}_e^{n+1} \Delta \gamma \right\}^T$ being the constitutive unknowns for this problem. Following \mathbf{C}_e^{n+1} , \mathbf{Q}_p^{n+1} is determined by (47), and the second Piola-Kirchhoff stress at step $n + 1$ is given in tensor notation by:

$$\begin{aligned} \check{\mathbf{S}}^{n+1} \left(\underbrace{\mathbf{C}_e^{n+1}}_{\mathbf{Y}}, \Delta \gamma \right) &= \mathbf{Q}_p^n \cdot \left[\Delta \widehat{\mathbf{Q}} \left(\mathbf{C}_e^{n+1}, \Delta \gamma \right) \right]^{-1} \cdot \widehat{\mathbf{S}}_e \left(\mathbf{C}_e^{n+1} \right) \\ &\cdot \left\{ \left[\Delta \widehat{\mathbf{Q}} \left(\mathbf{C}_e^{n+1}, \Delta \gamma \right) \right]^{-1} \right\}^T \cdot \left(\mathbf{Q}_p^n \right)^T. \end{aligned} \quad (52)$$

Stress sensitivity, the determination of the consistent modulus, with $\mathbf{S}^{n+1} = \text{Voigt}[\check{\mathbf{S}}^{n+1}]$, is determined as follows:

$$\frac{d\mathbf{S}^{n+1}}{d\mathbf{C}^{n+1}} = \frac{\partial \widehat{\mathbf{S}}^{n+1}}{\partial \mathbf{C}_e^{n+1}} \cdot \frac{d\mathbf{C}_e^{n+1}}{d\mathbf{C}^{n+1}} + \frac{\partial \widehat{\mathbf{S}}^{n+1}}{\partial \Delta \gamma} \frac{d\Delta \gamma}{d\mathbf{C}^{n+1}}. \quad (53)$$

In (53), a single product dot \cdot is adopted for double contraction of quantities in Voigt form. From (53), we can conclude that \mathcal{C} is determined as a function of the solution of (51), since:

$$d\mathbf{Y}/d\mathbf{C}^{n+1} = -\mathbf{J}^{-1} \cdot \frac{\partial \mathbf{r}}{\partial \mathbf{C}^{n+1}} \quad (54)$$

therefore, stress sensitivity is simply given by:

$$\frac{d\mathbf{S}^{n+1}}{d\mathbf{C}^{n+1}} = - (d\hat{\mathbf{S}}^{n+1}/d\mathbf{Y}) \cdot (d\mathbf{Y}/d\mathbf{C}^{n+1}). \quad (55)$$

The effective plastic strain rate follows the integration of (46):

$$\varepsilon_p^{n+1} = \varepsilon_p^n + \Delta\gamma \frac{\mathbf{T}_e : \mathbf{N}(\mathbf{T}_e)}{\sigma_y}. \quad (56)$$

4.3 Specific Yield Function

The nondimensional yield function is given by:

$$\phi_\star(\mathbf{T}_e) = \frac{\sigma_{\text{eq}}(\mathbf{T}_e)}{\sigma_y} - 1 \quad (57)$$

where, as a prototype equivalent stress, a specific Hill48 criterion (1948 [51]) is adopted. The general form of the Hill48 equivalent stress σ_{eq} is written as:

$$\sigma_{\text{eq}}(\mathbf{T}_e) = \left[F (T_{22} - T_{33})^2 + G (T_{33} - T_{11})^2 + H (T_{11} - T_{22})^2 \right. \quad (58)$$

$$\left. + 2S_1 (T_4^s)^2 + 2S_2 (T_5^s)^2 + 2S_3 (T_6^s)^2 \right]^{1/2} \quad (59)$$

where the subscript e of \mathbf{T}_e is omitted for conciseness. In (58), the superscript s is adopted to indicate a symmetrized quantity. For example, $T_6^s = 1/2 (T_{23} + T_{32})$. Introducing the yield ratios, $\mathbf{y} = \{y_1, \dots, y_6\}$ as constitutive data, we have for F, G, H, $S_{1,\dots,3}$:

$$F = \frac{1}{2} (1/y_2^2 + 1/y_3^2 - 1/y_1^2) \quad (60)$$

$$G = \frac{1}{2} (1/y_1^2 + 1/y_3^2 - 1/y_2^2)$$

$$H = \frac{1}{2} (1/y_1^2 + 1/y_2^2 - 1/y_3^2)$$

$$S_k = 3/2(y_{k+3}^2) \quad k = 3, \dots, 6.$$

We note that many other yield criteria can be used, since any specific form of $\sigma_{\text{eq}}(\mathbf{T}_e)$ can be inserted.

5 Numerical Tests

Numerical tests were performed with the code from the leading author, SimPlas [52], and the specific source code for \bar{C} -EFG was created using Mathematica [38] with the AceGen add-on [36, 39]. Source code for the equations in this work is available via GitHub [40].

5.1 Straight Cantilever Beam with Closed-Form Solution

We start with the Timoshenko and Goodier [53] cantilever beam in small strain elasticity. Two values of the Poisson coefficient are adopted: $\nu = 0.3$ and $\nu = 0.49999$. The quasi-incompressible case is here specified with a plane strain assumption. A comparison with the MINI element by D. Arnold [5] is performed. The beam is represented in Fig. 1.

We use the first slope boundary condition by Timoshenko and Goodier [53] who obtained the solution for the displacement in the plane stress case:

$$u(x, y) = \frac{P}{4c^3 E} \left\{ \begin{array}{l} \frac{E}{G} (y^3 - 3c^2 y) + 3y(l-x)(l+x) - \nu y^3 \\ (l-x)^2(2l+x) + 3\nu xy^2 \end{array} \right\}.$$

Introducing this solution into the strain components and making use of Hooke's law, we calculate the strain energy per unit thickness as:

$$U = \frac{1}{2} \int_0^l \left[\int_{-c}^{+c} (\varepsilon_{xx}\sigma_{xx} + \varepsilon_{yy}\sigma_{yy} + \gamma_{xy}\tau_{xy}) dy \right] dx. \quad (61)$$

The plane strain case is obtained replacing E by $E/(1-\nu^2)$ and ν by $\nu/(1-\nu)$. Strain energy per unit thickness is given by:

$$U_{\text{plane strain}} = \frac{P^2 [6c^2 El + 5Gl^3 (1 - \nu^2)]}{20c^3 GE}.$$

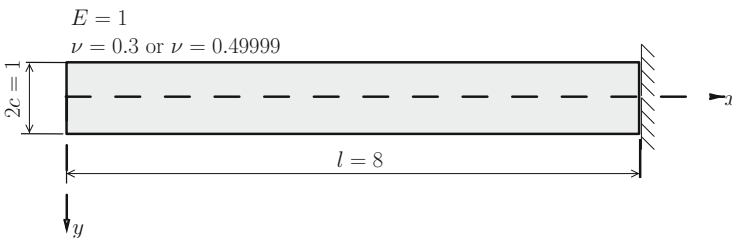


Fig. 1 Timoshenko and Goodier cantilever beam [53] with fixed support

Table 1 Closed-form and converged solutions for the cantilever beam

Closed-form solutions (specialized from [53])				
	Plane stress		Plane strain	
Poisson coefficient:	$v(0)$	U	$v(0)$	U
$\nu = 0.3$	2048	1036.48	1863.68	944.32
$\nu = 0.49999$	2048	1038.40	1536.02	782.41
Converged solutions ($h = 0.005$)				
	Plane stress		Plane strain	
Poisson coefficient:	$v(0)$	U	$v(0)$	U
$\nu = 0.3$	★	★	1880.90	940.33
$\nu = 0.49999$	★	★	1542.00	770.08

$$U_{\text{plane stress}} = \frac{P^2 (6c^2 El + 5Gl^3)}{20c^3 GE}.$$

Results are given in Table 1 for both cases. This table also shows the converged results for $h = 0.005$ obtained with a mixed finite element formulation [52]. Only the plane strain case will be addressed, since it is more demanding in terms of convergence.

Displacement results as a function of the characteristic mesh size h are summarized in Table 2, with the following cases being considered:

1. $\nu = 0.3$ with full quadrature (3 Gauss points per triangle for both C and \bar{C}).
2. $\nu = 0.49999$ with full quadrature.
3. $\nu = 0.49999$ with selective quadrature (3 Gauss points per triangle for C and 1 Gauss point for \bar{C}).

The following notation is adopted for the polynomials:

1. $1 \leq p_0 \leq 3$ is the degree of polynomial adopted for \bar{C} .
2. $1 \leq p_1 \leq 3$ with $p_1 \geq p_0$ is the degree of polynomial adopted for C .

From the observation of Table 2, we conclude that:

1. For the compressible case, all formulations behave acceptably, with the exception of $p_0 = p_1 = 1$ which results in excessive displacements. In addition, with $p_0 = p_1 = 2$, we can conclude that results are non-monotonous.
2. Using full quadrature for the quasi-incompressible case, two combinations exhibit severe volumetric locking: $p_0 = p_1 = 1$ and $p_0 = 1, p_1 = 2$.
3. Using selective quadrature for the quasi-incompressible case only $p_0 = 1, p_1 = 2$ exhibits locking. Both $p_0 = p_1 = 3$ and $p_0 = 2$ and $p_1 = 3$ are acceptable formulations.

Tip displacement error convergence is shown in Fig. 2 for $\nu = 0.3$ and $\nu = 0.49999$. The latter is considered with full and selective quadrature. Energy error convergence is determined for both the compressible and quasi-incompressible cases in Table 3 for $p_0 = 2$ and $p_1 = 3$.

Table 2 Timoshenko and Goodier cantilever beam: numerical results for $v(0)$

$\nu = 0.3$									
h	T3	MINI	$p_0 = 1, p_1 = 1$	$p_0 = 2, p_1 = 2$	$p_0 = 3, p_1 = 3$	$p_0 = 1, p_1 = 2$	$p_0 = 2, p_1 = 3$	$p_0 = 1, p_1 = 3$	$p_0 = 2, p_1 = 3$
0.0125	1880.3	1903.5	1891.4	1890.8	1884.0	1918.3	1887.6	1918.3	1887.6
0.0250	1878.5	1924.5	1901.8	1891.5	1883.9	1950.0	1890.7	1950.0	1890.7
0.0500	1871.5	1965.2	1943.3	1922.4	1886.8	2028.7	1904.4	2028.7	1904.4
0.1000	1842.4	2055.1	2059.9	1905.6	1887.6	2131.3	1909.8	2131.3	1909.8
0.2000	1758.6	2156.8	2478.1	1908.4	1901.6	2310.1	1964.4	2310.1	1964.4
$\nu = 0.49999$ full quadrature									
h	T3	MINI	$p_0 = 1, p_1 = 1$	$p_0 = 2, p_1 = 2$	$p_0 = 3, p_1 = 3$	$p_0 = 1, p_1 = 2$	$p_0 = 2, p_1 = 3$	$p_0 = 1, p_1 = 3$	$p_0 = 2, p_1 = 3$
0.0125	606.8	1554.1	1138.6	1531.1	1532.5	1136.4	1530.6	1136.4	1530.6
0.0250	277.4	1571.9	674.1	1525.5	1529.5	671.5	1524.0	671.5	1524.0
0.0500	208.8	1607.4	299.4	1509.8	1521.7	297.7	1505.7	297.7	1505.7
0.1000	185.1	1693.7	116.9	1453.4	1495.4	114.2	1445.4	114.2	1445.4
0.2000	166.9	1821.2	62.1	1277.0	1413.4	61.9	1260.8	61.9	1260.8
$\nu = 0.49999$ selective quadrature									
h	T3	MINI	$p_0 = 1, p_1 = 1$	$p_0 = 2, p_1 = 2$	$p_0 = 3, p_1 = 3$	$p_0 = 1, p_1 = 2$	$p_0 = 2, p_1 = 3$	$p_0 = 1, p_1 = 3$	$p_0 = 2, p_1 = 3$
0.0125	606.8	1554.1	1521.5	1534.1	1533.4	1517.8	1533.0	1517.8	1533.0
0.0250	277.4	1571.9	1478.5	1532.8	1531.5	1463.1	1530.0	1463.1	1530.0
0.0500	208.8	1607.4	1424.1	1531.7	1526.0	1369.6	1522.5	1369.6	1522.5
0.1000	185.1	1693.7	1059.6	1524.3	1514.8	885.0	1503.3	885.0	1503.3
0.2000	166.9	1821.2	1045.3	1493.5	1494.2	712.5	1445.8	712.5	1445.8

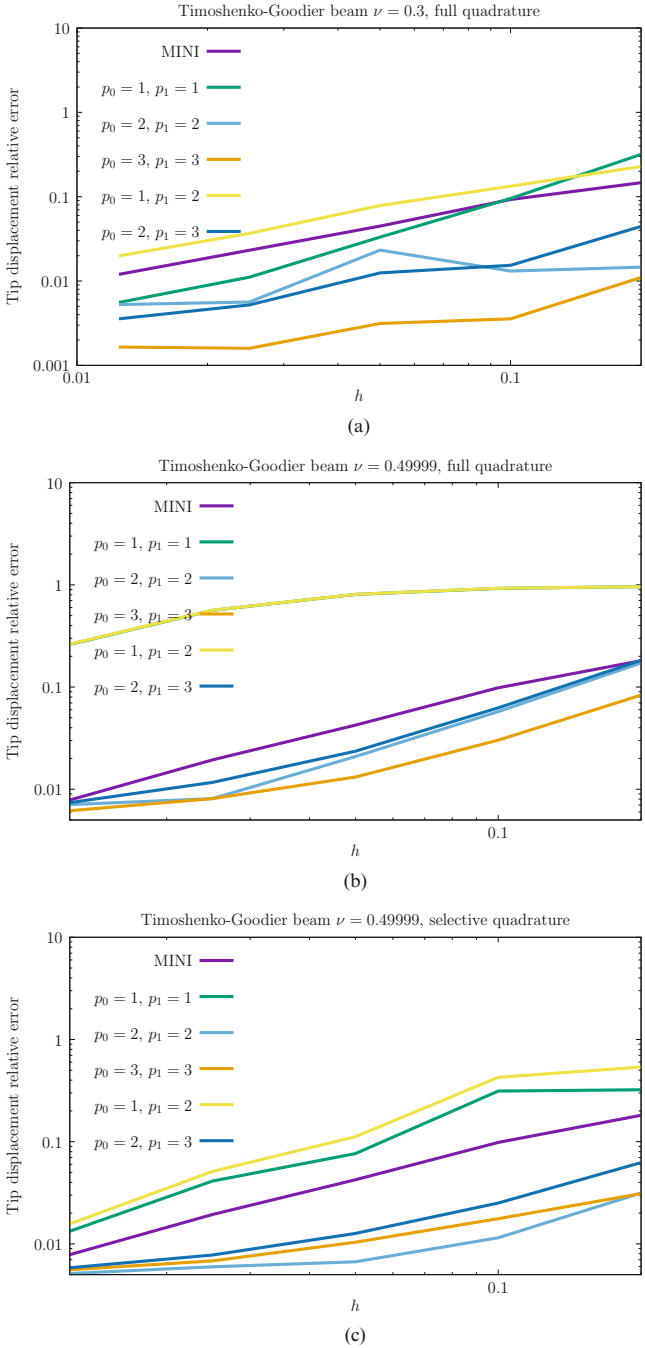


Fig. 2 Timoshenko-Goodier cantilever beam: tip displacement convergence for $\nu = 0.3$ and $\nu = 0.49999$. Results from the MINI element [5] are also included for comparison. (a) $\nu = 0.3$, full quadrature. (b) $\nu = 0.49999$, full quadrature. (c) $\nu = 0.49999$, selective quadrature

Table 3 Timoshenko and Goodier cantilever beam: numerical results for U in the plane strain case with selective quadrature and $p_0 = 2$ and $p_1 = 3$

h	$\nu = 0.3$	$\nu = 0.49999$
0.0125	943.7	766.5
0.0250	945.1	765.2
0.0500	949.5	762.1
0.1000	957.1	756.3
0.2000	981.8	743.5

Properties (**consistent units**):

$$E = 29870$$

$$\nu = 0.3$$

$$\sigma_y = 41 + 205\bar{\varepsilon}_p \text{ (linear hardening case)}$$

$$\sigma_y = 112(\bar{\varepsilon}_p + 0.0113)^{0.227} \text{ (power law case)}$$

Nodes:

535 nodes

868 nodes

3616 nodes

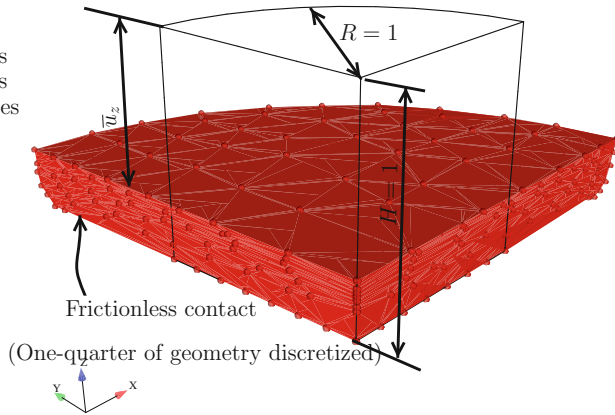


Fig. 3 Billet upsetting test: relevant data and notation

5.2 Billet Upsetting Test

We make use of the upsetting test reported by M.A. Puso and J. Solberg [54] in its two elastoplastic versions (linear and power hardening). Geometry, boundary conditions, and constitutive properties are shown in Fig. 3. Three uniform meshes are adopted for comparison, containing 535, 868, and 3616 nodes. Nodes are forced to remain above a horizontal plane by a non-penetration condition. Of the two cases reported in [54], the elastoplastic case described is the most demanding, and it was found that only their nodal integrated and stabilized UT4s provided stable and accurate results. Using a cubic basis ($p_0 = p_1 = 3$), Fig. 4 shows the very smooth contour plots for ε_p and hydrostatic σ_H . All three factors contribute to a more flexible behavior: finer meshes are less stiff, larger supports produce softer behavior, and quadratic basis produces results beneath the reaction displacement curve reported in [54]. Using uniform quadrature and uniform interpolation, Fig. 5 shows the results compared with the reported in [54]. We test three basis dimensions:

Power-law hardening case

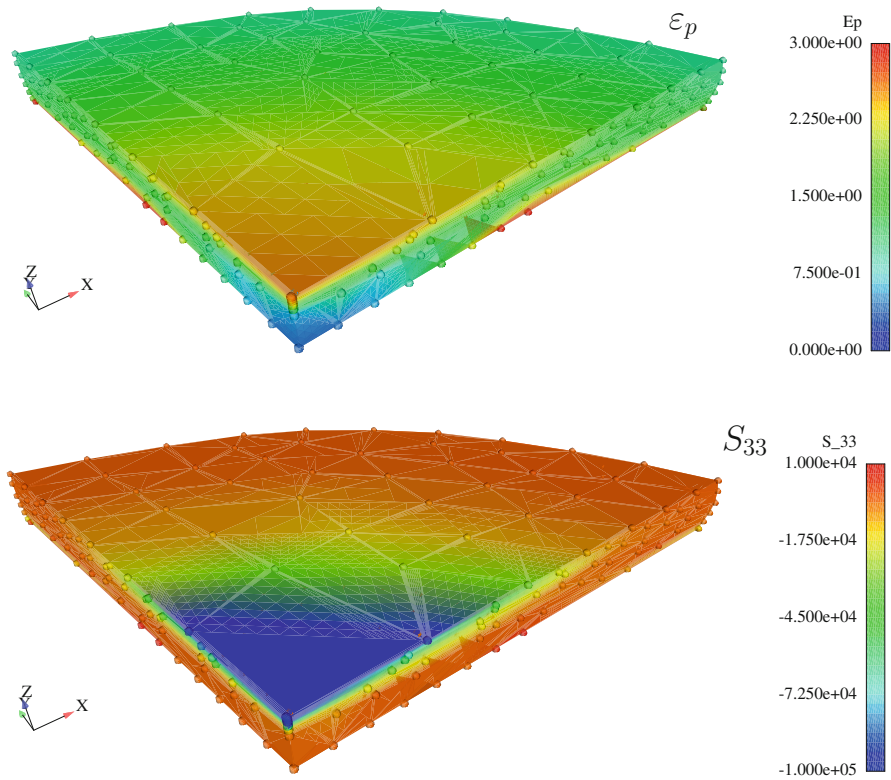


Fig. 4 Upsetting test: contour plots (ϵ_p, S_{33}) for the power-law hardening case and 535 nodes

linear, quadratic, and cubic with $n = 25$. In terms of quadrature, both 1 and 4 Gauss points are tested. Reduced quadrature produces exceedingly flexible results, as shown in Fig. 5. This conclusion leads us to favor either full quadrature (4 points in both terms) or selective quadrature (4 points for the deviatoric terms and 1 point for the volumetric term). Focusing on the polynomial bases, Fig. 6 shows the effect of p_0 and p_1 on the displacement-reaction behavior. The following conclusions are taken:

- In contrast with displacement-based finite elements, increasing the polynomial degree does not produce more flexible results.
- In contrast with finite elements, uniform reduced quadrature does not produce hourglassing/point instabilities. However, significant loss of stiffness is observed, which precludes its use in the quasi-incompressible case.

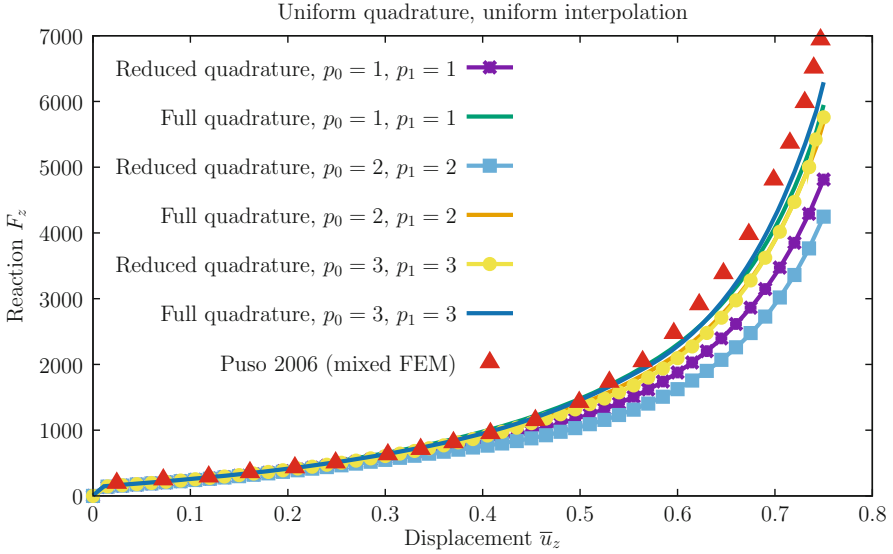


Fig. 5 Upsetting test, linear hardening, $n = 25$: effect of dimension of polynomial basis for uniform quadrature/uniform basis

- The polynomial degree of the deviatoric term, p_1 , is important in terms of results.

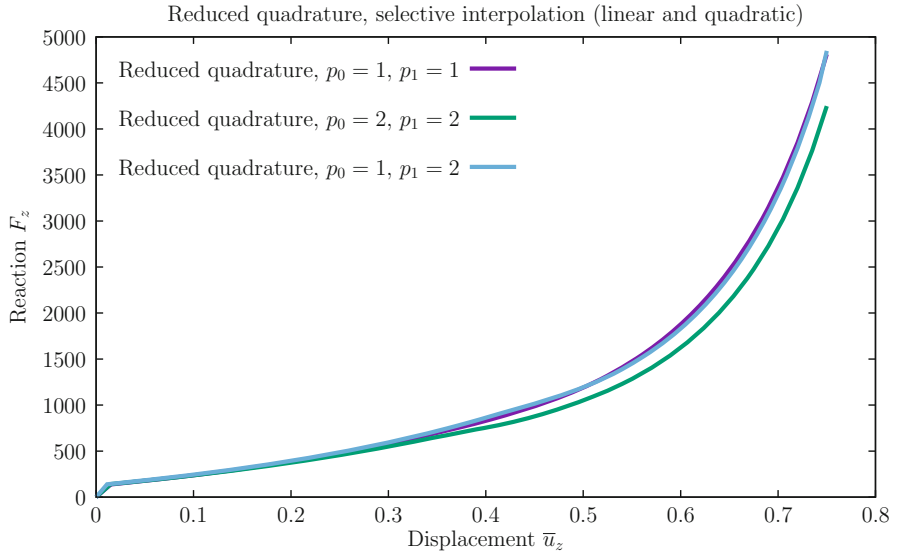
Selective interpolation is now contemplated, with Fig. 7 showing the effect of combining distinct bases. We conclude that the deviatoric term p_1 is crucial for the results.

Combining selective quadrature with full interpolation, results show that significant differences exist by changing the basis (see Fig. 8). In terms of mesh convergence, excellent results are obtained, as Fig. 9 shows. In our experience, this is one of the advantages of meshless methods.

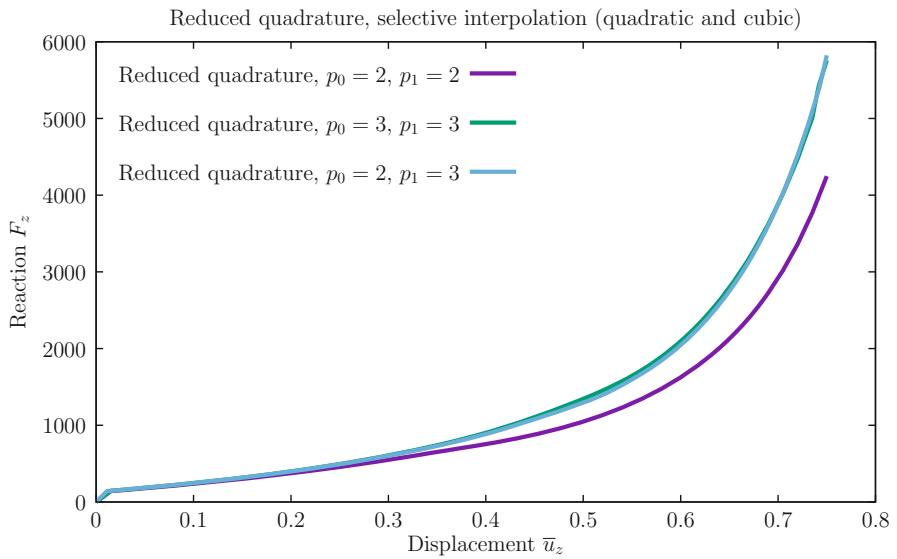
Finally, to complete the test of Puso and Solberg [54], the power-law hardening is tested in Fig. 10

5.3 Tension Test

We apply the \bar{C} -EFG method to the tension test discussed by Simo and co-workers in the context of J_2 plasticity [9] (see also the 1993 reference [55] where the test is described in detail). Geometry, boundary conditions, and material properties are summarized in Fig. 11, along with the two cases of nodal distribution, structured and unstructured, as this was found to have an effect on the results. The contour plot



(a)



(b)

Fig. 6 Upsetting test, $n = 25$, effect of selective polynomial basis for the deviatoric (p_1) and volumetric (p_0) terms. Reduced quadrature. (a) Linear and quadratic bases. (b) Quadratic and cubic bases. (c)

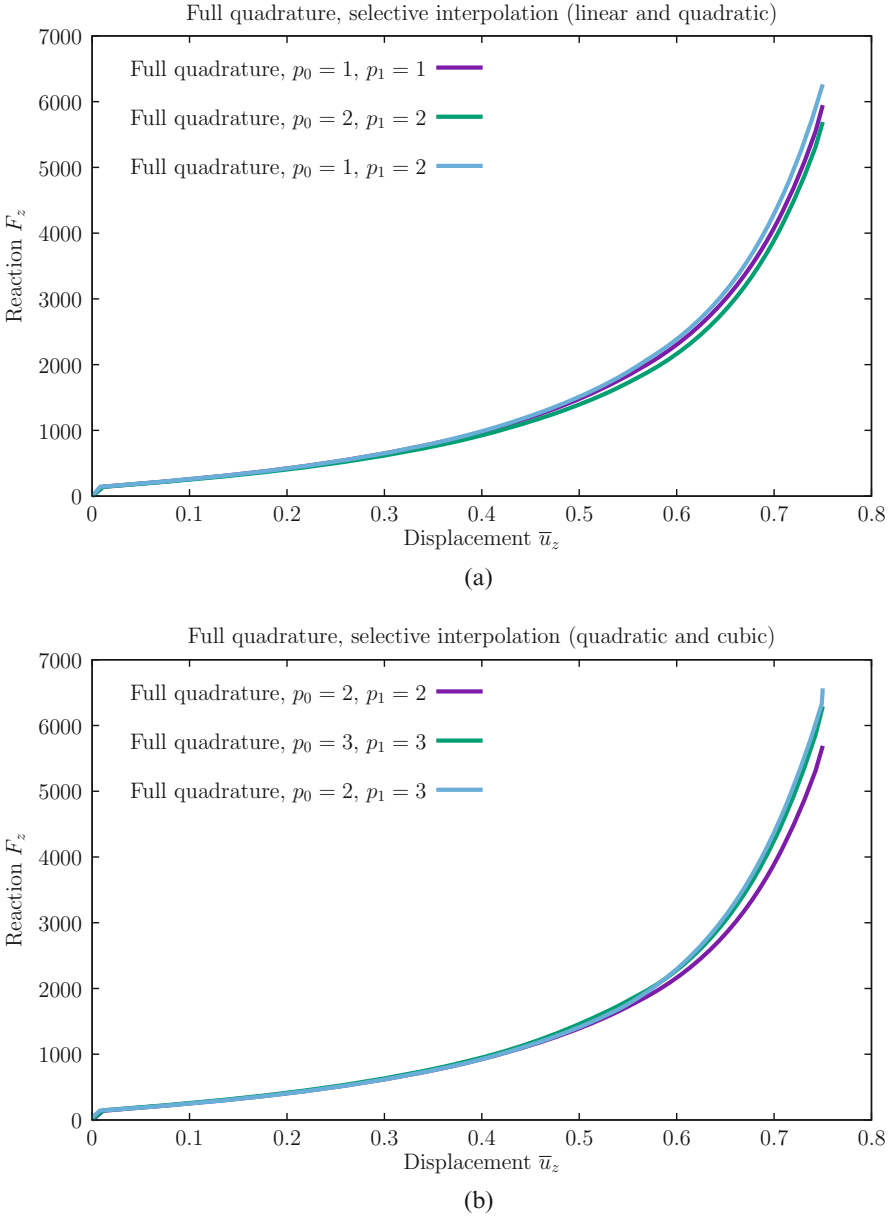


Fig. 7 Upsetting test, $n = 25$, effect of selective polynomial basis for the deviatoric (p_1) and volumetric (p_0) terms. Full quadrature. (a) Linear and quadratic bases. (b) Quadratic and cubic bases

of the effective plastic strain, given by Eq. (56), is shown in Fig. 12 for two values of \mathbf{y} . The specific yield stress σ_y is given by the hardening law shown in Fig. 11.

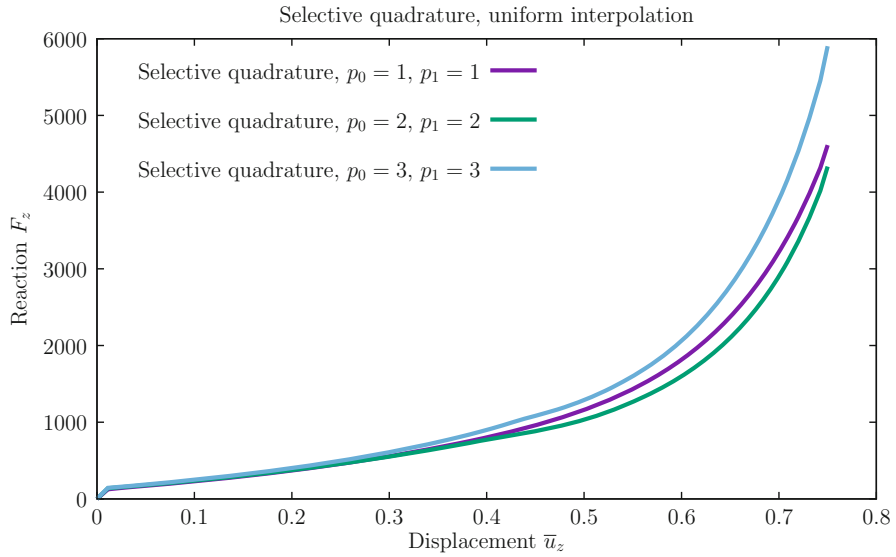


Fig. 8 Upsetting test, $n = 25$, effect of selective quadrature for uniform interpolation

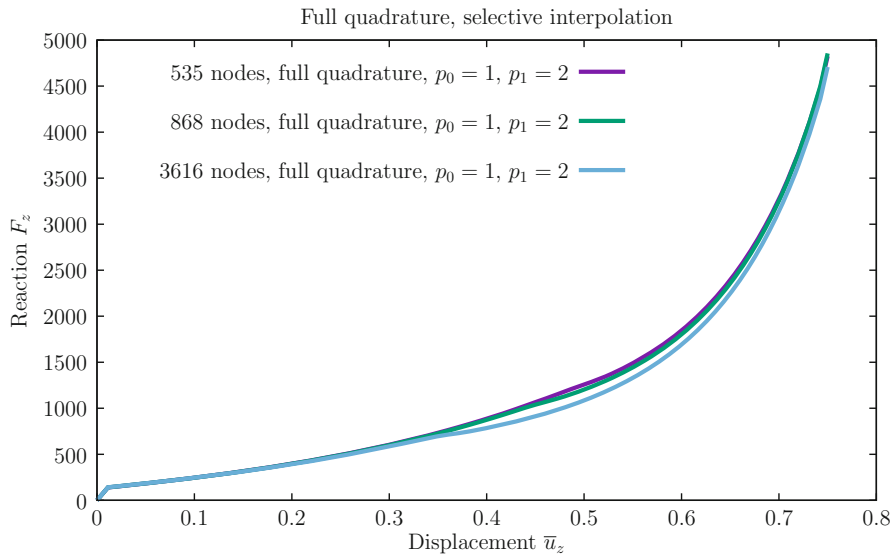


Fig. 9 Effect of a number of nodes using full quadrature and selective interpolation

Compared to mixed FE formulations, results are distinct. When compared with enhanced assumed strain hexahedra, specifically Simo and Armero [7, 55], both the initial plastic behavior and the post-localization behavior are different (see Fig. 13). We note that two significant differences exist: (1) Simo and Armero adopted a

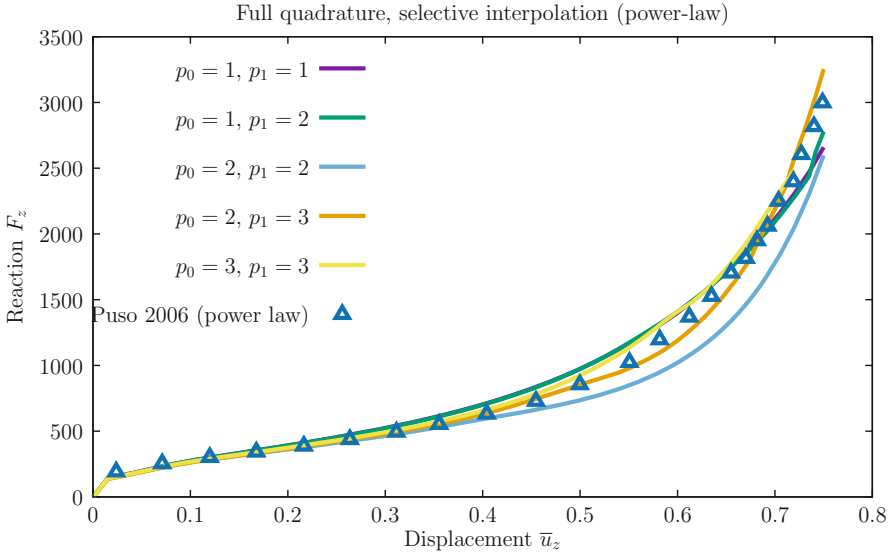


Fig. 10 Results for power-law hardening

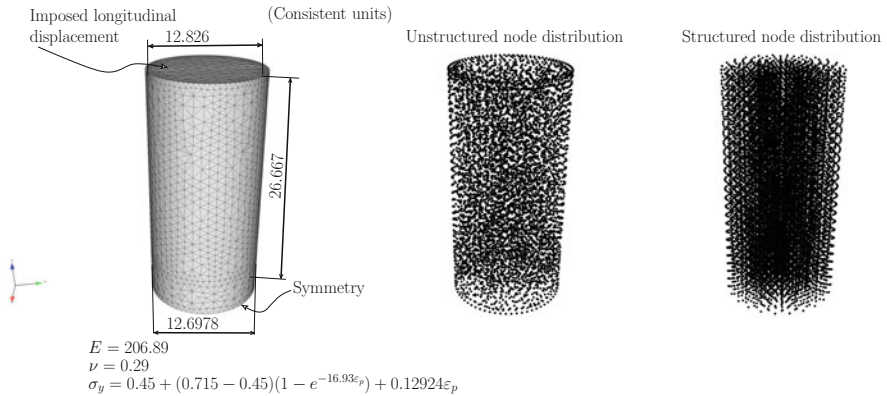


Fig. 11 Relevant dimensions and mesh for the Neo-Hookean/Hill48 tension test

formulation based on the Kirchhoff stress tensor and radial-return mapping for J_2 plasticity and (2) hexahedra tend to reproduce the incompressibility condition with sharper stretching. MINI elements (see, [5]) are also used for comparison, as Fig. 13 shows. When compared with the MINI runs, much coarser meshes are used in EFG for similar results. In contrast with the previous examples, finer node distributions result in a sharper localization region, with lower reactions for higher displacements. For the structured mesh with 3760 nodes, Fig. 14a shows the advantages of using $p_0 = 2$ and $p_1 = 3$ in terms of post-localization. When adopting an unstructured

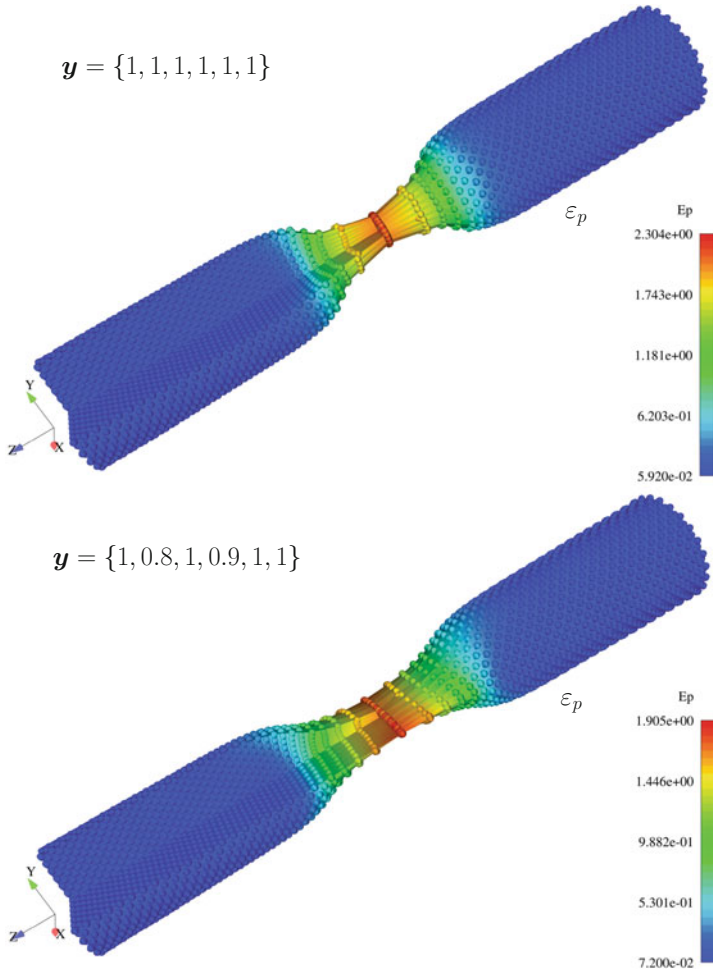


Fig. 12 Tension test: deformed configurations for both yield functions ($\{1, 1, 1, 1, 1, 1\}$ and $\{1, 0.8, 1, 0.9, 1, 1\}$) with the corresponding effective plastic strain colors

node distribution, a less pronounced post-localization behavior is exhibited (see Fig. 14b).

6 Conclusions

In the context of \bar{C} decomposition and by parameterizing the quadrature and the degree of the polynomial basis, we developed a discretization scheme with the following distinctive features:

Tension test, reduced quadrature and selective interpolation. Structured node distribution

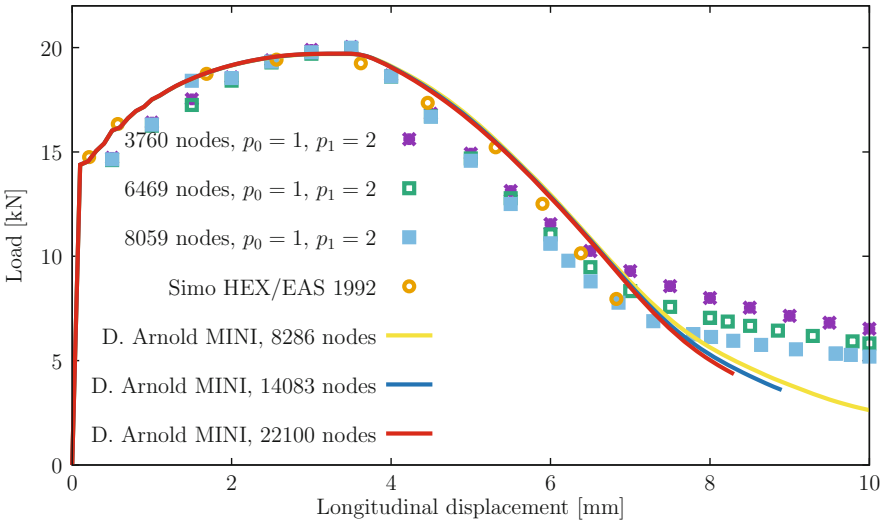


Fig. 13 Comparison with advanced finite element technology [7, 55] and effect of node density on the results

- An initial perturbation of internal FE nodal positions is performed for efficiency reasons (low n).
- From linear up to cubic shape, functions are adopted for the volumetric and deviatoric terms of the right Cauchy-Green tensor. Lagrangian diffuse derivatives are defined ab initio for the entire analysis.
- A pre-established nodal support is imposed, and a tetrahedra integration with 1 or 4 quadrature points for \mathbf{C} and $\bar{\mathbf{C}}$ is adopted.
- Constitutive integration makes use of the Mandel stress tensor and iteration on \mathbf{C}_e [16].

Implementation is straightforward and was performed in SimPlas [52] with AceGen [39] and Mathematica [38]. Three benchmark tests were performed, which allow the following conclusions:

- Even with small supports and coarse meshes, results are highly competitive with established finite elements if either selective interpolation or selective quadrature are adopted. This holds for the quasi-incompressible case where special finite elements are adopted.
- Numerical testing shows that the ideal combination is $p_0 = 2$ and $p_1 = 3$ with either selective or full quadrature.
- Finite strain plasticity solutions are very robust, with large strains being possible without loss of convergence or instabilities.
- The finite strain formulation is simpler than with mixed finite elements and on par with displacement-based FEM. Source code is available at GitHub, cf. [40].

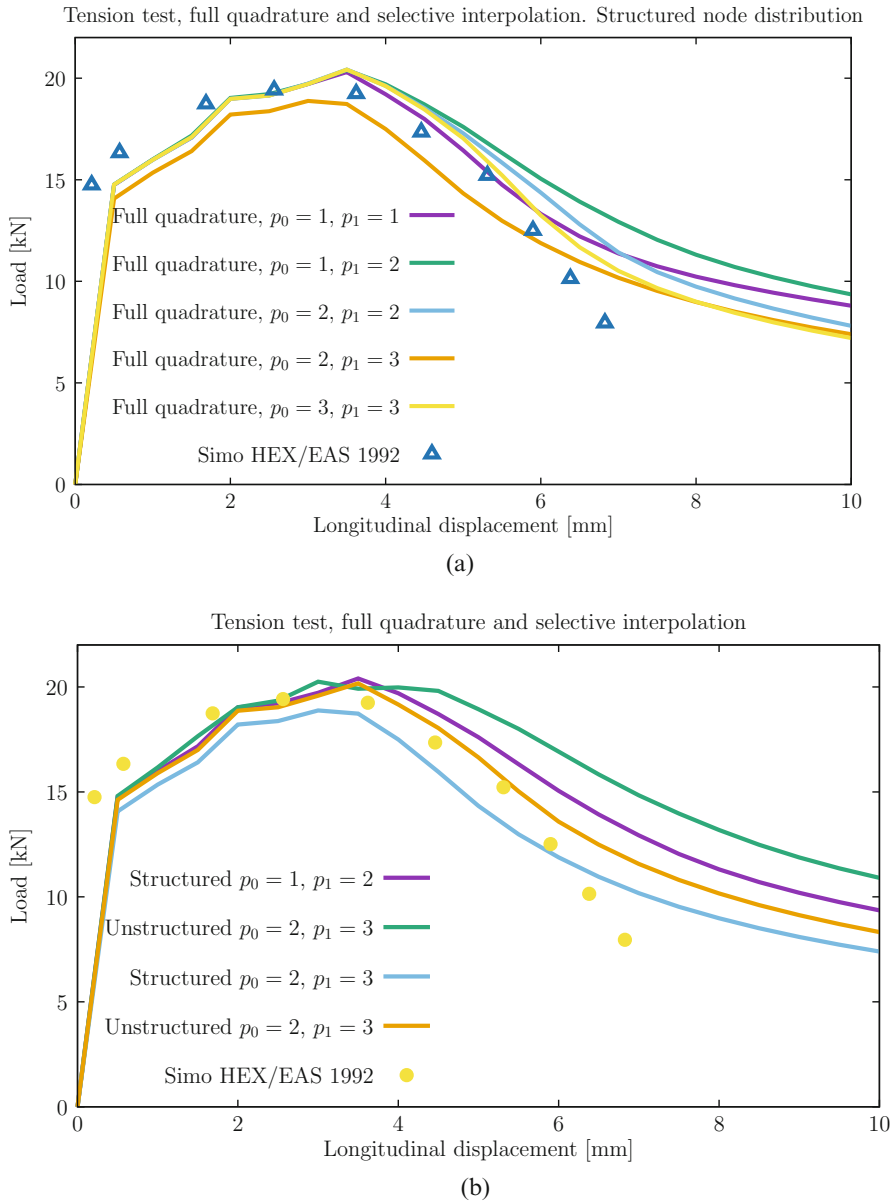


Fig. 14 Effect of selective interpolation and structured/unstructured node distribution. (a) Effect of selective interpolation. (b) Effect of structured/unstructured node distribution

Acknowledgments The authors acknowledge the support of FCT, through IDMEC, under LAETA, project UIDB/50022/2020.

Appendix

First and Second Variations of $\det [\mathbf{C}]$

For the determinant of \mathbf{C} , the following relations hold, which follow from established results and application of the chain rule:

$$\delta \det [\mathbf{C}] = \det [\mathbf{C}] \mathbf{C}^{-1} : \delta \mathbf{C} \quad (62)$$

$$\begin{aligned} d\delta \det [\mathbf{C}] &= d\mathbf{C} : \left(\det [\mathbf{C}] \mathbf{C}^{-1} \otimes \mathbf{C}^{-1} \right) : \delta \mathbf{C} \\ &+ \det [\mathbf{C}] : d\delta \mathbf{C} - d\mathbf{C} : \mathbb{S} : \delta \mathbf{C} \end{aligned} \quad (63)$$

where \mathbb{S} is a fourth-order tensor with components $S_{kl ij} = C_{ik}^{-1} C_{lj}^{-1}$. Given the n -th power of $\det [\mathbf{C}]$, $\det [\mathbf{C}]^n$, it follows that:

$$\delta \det [\mathbf{C}]^n = n \det [\mathbf{C}]^{n-1} \delta \det [\mathbf{C}] \quad (64)$$

$$d\delta \det [\mathbf{C}]^n = n(n-1) \det [\mathbf{C}]^{n-2} \delta \det [\mathbf{C}] d\det [\mathbf{C}] + n \det [\mathbf{C}]^{n-1} d\delta \det [\mathbf{C}] \quad (65)$$

with $\delta \det [\mathbf{C}]$ being given by (62) and $d\delta \det [\mathbf{C}]$ by (63). Given $\theta_C = \det [\bar{\mathbf{C}}]$, similar expressions are obtained for $\delta\theta_C$ and $d\delta\theta_C$.

References

1. N.S. Lee, K.J. Bathe, Effects of element distortions on the performance of isoparametric elements. *Int. J. Numer. Meth. Eng.* **36**, 3553–3576 (1993)
2. J. Dolbow, N. Moës, T. Belytschko, Modeling fracture in Mindlin-Reissner plates with the extended finite element method. *Int. J. Solids Struct.* **37**, 7161–7183 (2000)
3. X. Peng, E. Atroshchenko, P. Kerfriden, S.P.A. Bordas, Isogeometric boundary element methods for three dimensional static fracture and fatigue crack growth. *Comp. Method. Appl. Mech. Eng.* **316**, 151–185 (2017)
4. K.-J. Bathe, *Finite Element Procedures* (Prentice-Hall, Hoboken, 1996)
5. D.N. Arnold, F. Brezzi, M. Fortin, A stable finite element for the Stokes equations. *Calcolo* **XXI**(IV), 337–344 (1984)
6. J.C. Simo, R.L. Taylor, K.S. Pister, Variational and projection methods for the volume constraint in finite deformation elastoplasticity. *Comp. Method. Appl. Mech. Eng.* **51**, 177–208 (1985)
7. J.C. Simo, F. Armero, Geometrically non-linear enhanced strain mixed methods and the method of incompatible modes. *Int. J. Numer. Meth. Eng.* **33**, 1413–1449 (1992)
8. T. Rabczuk, T. Belytschko, S.P. Xiao, Stable particle methods based on Lagrangian kernels. *Comp. Method Appl. Mech. Eng.* **193**, 1035–1063 (2004)

9. J.C. Simo, Algorithms for static and dynamic multiplicative plasticity that preserve the classical return mapping schemes of the infinitesimal theory. *Comp. Method Appl. Mech. Eng.* **99**, 61–112 (1992)
10. J.C. Simo, T.J.R. Hughes, *Computational Inelasticity*, Corrected Second Printing Edition (Springer, Berlin, 2000)
11. R. Rossi, M.K. Alves, On the analysis of an EFG method under large deformations and volumetric locking. *Comput. Mech.* **39**, 381–399 (2007)
12. J.-S. Chen, M. Hillman, S.-W. Chi, Meshfree methods: Progress made after 20 years. *J. Eng. Mech-ASCE* **143**(4), 04017001 (2017)
13. Y. Cai, X. Zhuang, C. Augarde, A new partition of unity finite element free from the linear dependence problem and possessing the delta property. *Comp. Method Appl. Mech. Eng.* **199**, 1036–1043 (2010)
14. B. Boroomand, S. Parand, Towards a general interpolation scheme. *Comp. Method Appl. Mech. Eng.* **381**, 113830 (2021)
15. G. Bourantas, B.F. Zwick, G.R. Joldes, A. Wittek, K. Miller, Simple and robust element-free Galerkin method with almost interpolating shape functions for finite deformation elasticity. *Appl. Math. Model* **96**, 284–303 (2021)
16. P. Areias, T. Rabczuk, J. Ambrósio, Extrapolation and c_e -based implicit integration of anisotropic constitutive behavior. *Int. J. Numer. Meth. Eng.* **122**, 1218–1240 (2021)
17. A. Huerta, S.F. Méndez, Locking in the incompressible limit for the element-free galerkin method. *Int. J. Numer. Meth. Eng.* **51**, 1361–1383 (2001)
18. P. Lancaster, K. Salkauskas, Surfaces generated by moving least squares methods. *Math. Comput.* **37**(155), 141–158 (1981)
19. T. Most, C. Bucher, A moving least squares weighting function for the element-free Galerkin method which almost fulfills essential boundary conditions. *Struct. Eng. Mech.* **21**(3), 315–332 (2005)
20. T. Most, C. Bucher, New concepts for moving least squares: an interpolation non-singular weighting function and weighted nodal least squares. *Eng. Anal. Bound Elem.* **32**, 461–470 (2008)
21. J. Dolbow, T. Belytschko, Volumetric locking in the element free galerkin method. *Int. J. Numer. Meth. Eng.* **46**, 925–942 (1999)
22. J.-S. Chen, S. Yoon, H.-P. Wang, W.K. Liu, An improved reproducing kernel particle method for nearly incompressible finite elasticity. *Comp. Method Appl. Mech. Eng.* **181**, 117–145 (2000)
23. C.-T. Wu, S.-W. Chi, M. Koishi, Y. Wu, Strain gradient stabilization with dual stress points for the meshfree nodal integration method in inelastic analyses. *Int. J. Numer. Meth. Eng.* **107**, 3–30 (2016)
24. D.P. Recio, R.M. Natal Jorge, L.M.S. Dinis, Locking and hourglass phenomena in an element-free Galerkin context: the B-bar method with stabilization and an enhanced strain method. *Int. J. Numer. Meth. Eng.* **68**, 1329–1357 (2006)
25. W.M. Coombs, T.J. Charlton, M. Cortis, C.E. Augarde, Overcoming volumetric locking in material point methods. *Comp. Method Appl. Mech. Eng.* **333**, 1–21 (2018)
26. G. Moutsanidis, J.J. Koester, M.R. Tupek, J.-S. Chen, Y. Bazilevs, Treatment of near-incompressibility in meshfree and immersed-particle methods. *Comput. Part Mech.* **7**, 309–327 (2020)
27. P. Navas, S. López-Querol, R.C. Yu, B. Li, B-bar based algorithm applied to meshfree numerical schemes to solve unconfined seepage problems through porous media. *Int. J. Numer. Meth. Eng.* **40**, 962–984 (2016)
28. T. Belytschko, Y.Y. Lu, L. Gu, Element-free galerkin methods. *Int. J. Numer. Meth. Eng.* **37**, 229–256 (1994)
29. T. Belytschko, Y. Krongauz, D. Organ, M. Fleming, P. Krysl, Meshless methods: an overview and recent developments. *Comp. Method Appl. Mech. Eng.* **139**, 3–47 (1996)
30. G.J. Golub, C.F. Van Loan, *Matrix Computations*, 3rd edn. (Johns Hopkins, Baltimore, 1996)
31. P. Areias, EFG MLS (2021). <https://github.com/PedroAreiasIST/EFG>

32. B. Nayroles, G. Touzot, P. Villon, Generalizing the finite element method: Diffuse. *Comput. Mech.* **10**, 307–318 (1992)
33. M. Dehghan, M. Abbaszadeh, Interpolating stabilized moving least squares (MLS) approximation for 2D elliptic interface problems. *Comp. Method Appl. Mech. Eng.* **328**, 775–803 (2018)
34. B. Moran, M. Ortiz, C.F. Shih, Formulation of implicit finite element methods for multiplicative finite deformation plasticity. *Int. J. Numer. Meth Eng.* **29**, 483–514 (1990)
35. J.C. Nagtegaal, D.M. Parks, J.R. Rice, On numerically accurate finite element solutions in the fully plastic range. *Comp. Method Appl. Mech. Eng.* **4**, 153–177 (1974)
36. P. Wriggers, *Nonlinear Finite Element Methods* (Springer, Berlin, 2008)
37. P.J. Flory, Elasticity of polymer networks cross-linked in states of strain. *Trans. Faraday Soc.* **56**, 722–743 (1960)
38. Wolfram Research Inc. *Mathematica* (2007)
39. J. Korelc, Multi-language and multi-environment generation of nonlinear finite element codes. *Eng. Comput.* **18**(4), 312–327 (2002)
40. P. Areias, F-bar in meshless (2020). <https://github.com/PedroAreiasIST/fbar>
41. T. Belytschko, W.K. Liu, B. Moran, *Nonlinear Finite Elements for Continua and Structures* (Wiley, Hoboken, 2000)
42. P. Areias, J.M.A. César de Sá, C.A. Conceição António, A.A. Fernandes, Analysis of 3D problems using a new enhanced strain hexahedral element. *Int. J. Numer. Meth Eng.* **58**, 1637–1682 (2003)
43. P. Areias, C. Tiago, J. Carrilho Lopes, F. Carapau, P. Correia, A finite strain Raviart-Thomas tetrahedron. *Eur. J. Mech. A-Solid* **80**, 103911 (2020)
44. J. Mandel, Equations constitutives et directeurs dans les milieux plastiques et viscoplastiques. *Int. J. Solids Struct.* **9**, 725–740 (1973)
45. B. Eidel, F. Gruttmann, Elastoplastic orthotropy at finite strains: multiplicative formulation and numerical implementation. *Comput. Mater. Sci.* **28**, 732–742 (2003)
46. E. Kröner, Allgemeine kontinuumstheorie der versetzungen und eigenspannungen. *Arch. Ration Mech. Anal.* **4**, 273–334 (1960)
47. E.H. Lee, Elasto-plastic deformation at finite strains. *J. Appl. Mech.-ASME* **36**, 1–6 (1969)
48. J. Lubliner, *Plasticity Theory* (Macmillan, London, 1990)
49. M.E. Gurtin, *An Introduction to Continuum Mechanics*. Mathematics in Science and Engineering, vol. 158 (Academic, New York, 1981)
50. J. Mandel, *Foundations of Continuum Thermodynamics*, Chapter Thermodynamics and Plasticity (MacMillan, London, 1974), pp. 283–304
51. R. Hill, A theory of yielding and plastic flow of anisotropic metals. *Proc. R. Soc. Lond.* **193**, 281–297 (1948)
52. P. Areias, Simplas. <http://www.simplassoftware.com>. Portuguese Software Association (ASSOFT) registry number 2281/D/17.
53. S. Timoshenko, J.N. Goodier, *Theory of Elasticity*, 2nd edn. (McGraw-Hill Book Company, New-York, 1951)
54. M.A. Puso, J. Solberg, A stabilized nodally integrated tetrahedral. *Int. J. Numer. Methods Eng.* **67**, 841–867 (2006)
55. J.C. Simo, F. Armero, R.L. Taylor, Improved versions of assumed strain tri-linear elements for 3D finite deformation problems. *Comp. Method Appl. Mech. Eng.* **110**, 359–386 (1993)